applied sciences

MDPI

Article

In-Cylinder Heat Transfer Model Proposal Compatible with 1D Simulations in Uniflow Scavenged Engines

Héctor Climent, Andrés Tiseira, Josep Gomez-Soriano and Aditya Darbhamalla *

CMT Motores Térmicos, Universitat Politècnica de València, Camino de Vera s/n, 46022 Valencia, Spain
* Correspondence: adarbha@mot.upv.es; Tel.: +34-96-387-76-50

Abstract: Advanced two-stroke engines are considered as powertrains for range extenders in hybrid electric vehicles due to size, simplicity, cost, and power density advantages. In-cylinder heat transfer is a phenomenon that affects the temperature of burnt gases and fresh air in an internal combustion engine. Compared to four-stroke units, this influence is more critical in two-stroke engines during the scavenging process since the gases velocity field inside the cylinder evolves rapidly in space and time. This study proposes a new convective heat transfer coefficient model beyond those based on Reynolds number calculation with the mean piston velocity. The model uses semi-empirical equations with non-dimensional numbers since it has to be integrated within the frame of a physical engine model, where thermo- and fluid dynamic properties of the gases inside the engine are solved using 0D or 1D approaches. In this particular application, the temperature deviation led to a poor prediction of trapped mass in the cylinder. The proposed convective heat transfer coefficient is calculated using a pseudo-velocity of the gases inside the cylinder based on the mass flow rates in the intake and exhaust ports during scavenging. The experimental results validate the 1D engine physical model, which is then used as initial conditions for CFD simulations. These CFD results are used to deduce the necessary conclusions for enhanced temperature predictability during scavenging, where deviations of less than 2% can be observed and an impact of up to 12% on the in-cylinder trapped mass can be seen.

Keywords: heat transfer; two-stroke powertrains; range extender; scavenging

Citation: Climent, H.; Tiseira, A.; Gomez-Soriano, J.; Darbhamalla, A. In-Cylinder Heat Transfer Model Proposal Compatible with 1D Simulations in Uniflow Scavenged Engines. *Appl. Sci.* **2023**, *13*, 3996. https://doi.org/10.3390/app13063996

Academic Editor: Adrian Irimescu

Received: 7 March 2023
Revised: 16 March 2023
Accepted: 17 March 2023
Published: 21 March 2023

1. Introduction

Automotive engineering is moving towards sustainable mobility to reduce the emission of greenhouse gases. This change in emissions regulation has led to the development of new engine designs and concepts. Extensive research is being conducted in two-stroke and four-stroke engines for improvements to produce electricity and for sustainable mobility. The working fluid used in these novel engines is either diesel, gasoline, advanced fuels, or a combination of fuels, as depicted by García-Oliver et al. [1]. One such engine is assessed for novel piston movement, like a rocker arm, called a crank rocker engine, where the combustion chamber and piston have a curvature as depicted in [2] and produce the necessary high power density output. Serrano et al. [3] assessed a rodless concept of a two-stroke engine to meet future emission standards requirements. Mikalsen et al. [4] have presented a new type of turbocharged free-piston engine with diesel as the working fuel and, and results have shown a reduction in the production of nitrogen oxides. A comparative study on free-piston engines performed with both two-stroke and four-stroke engines is presented in [5], showing results on the advantages and disadvantages of the performance of the engine type. Mikalsen et al. [6] have reviewed different types of free-piston engines and their applications and evaluated the potential of the free piston for its most promising design. Mikalsen et al. [7] performed CFD analysis on free-piston engines and compared the results with conventional engines, revealing the free-piston engine's potential. Herold et al. [8] presented a three-cylinder opposed-piston configuration in two-stroke

and four-stroke setups and compared the results with a heavy-duty engine. Results show that the two-stroke engine configuration leads to approximately 9% lower brake-specific fuel consumption. Furthermore, electric vehicles are being extensively studied for battery thermal management. Buidin et al. [9] studied the effect of a higher heat transfer coefficient for accurate prediction of battery performance.

The primary research focus of the two-stroke engine is to attain higher scavenging and improve the engine's performance. To attain higher scavenging, Wang et al. [9] optimized several parameters such as bore-stroke ratio, intake scavenging ports, and intake design, and have proven improved brake thermal efficiency using CFD analysis. A hybrid air operation assessment was performed for the same engine configuration to attain higher scavenging efficiency [10]. Once the engine parameters were optimized, the same research group assessed the engine with a turbocharger and presented results with enhanced brake power and torque [11]. The same scientist has also evaluated the effect of piston-shape design for enhanced scavenging and lower fuel consumption [12]. Benson et al. [13] have quantitively assessed a mixing displacement method to improve scavenging, thereby improving charging efficiency in a two-stroke engine. Research is not only limited to down-sized engines; marine engines are also tested for higher performance. Sakellaridis et al. [14] analyzed a marine two-stroke engine with a turbocharger and presented improved engine performance. Other researchers have also studied the effect of ignition timing for higher performance and lower emission in an SI two-stroke engine [15]. A three-phase scavenging model in a marine engine was studied using 2D CFD, and results are presented in [16]. Zhu et al. [17] studied different air control methods to assess a marine two-stroke engine for enhancement in scavenging. Kim et al. [18] studied a marine engine's spray angle and injection position for optimum engine performance for low emissions.

Although the determination of improved scavenging is measured in terms of enhanced engine performance, only a few researchers have studied how to estimate the trapped mass inside the cylinder. This estimation technique uses in-cylinder pressure traces to determine the trapped mass, as depicted by Bares et al. [19]. Carlucci et al. [20] have presented an inexpensive way to predict trapped mass by considering the molar concentration of CO_2 and oxygen in the tailpipe. Leo et al. [21] proposed a technique in which experimental in-cylinder traces were used to calculate the trapped mass; their predictive methodology also depicts the air-to-fuel ratio. Using air mass flow and lambda sensors, Arsie et al. [22] predicted the trapped mass and air-to-fuel ratio and compared the results with the in-cylinder pressure method, and stated a high accuracy of predictability.

Advanced two-stroke engines are being studied for their potential to lower emissions for sustainable mobility. This can be attributed to the compactness of the engine, which can be heavily downsized, and have fewer emissions due to their design and operating range. Extensive literature is available with results for the initialization of the free piston to control pollutants. These assessments mainly focus on simulation, where the engine models are calibrated using the respective engine prototype's experimental results. For the control of a free piston, a fast response dynamic model is presented by Jia et al. [23]. The above simplified model has shown advantages in extensive studies as it could be coupled to any computing software and real-time hardware in the loop. The same research group in [24] presented sub-models for the process of starting a free-piston engine generator along with steady-state operation, considering heat transfer correlations and air leaks, and used the model to study various starting motor forces and combustion processes. Jia et al. [25] have presented results with resonance-based actuation of free-piston engines and have shown improved model prediction of experimental results while comparing the results with dynamic modeling. Cha et al. [26] have studied the effect of in-cylinder thermodynamics due to combustion and presented critical observations for isentropic expansion and kinetic energy recovery. Jia et al. [27] proposed a new cascade model to control the free piston and have shown improved peak prediction and settling time. Li et al. [28] have assessed a feedforward controller for tracking performance and compared the results with experimental data to demonstrate the effectiveness of the feedforward

control. Feng et al. [29] have implemented a switching strategy between motor/generator power to start the free-piston engine to a steady state. Dizo et al. [30] studied a prototype engine with rotating cylinders powered by compressed air and depicted the disadvantages of such engines over conventional combustion engines. Kim et al. [31] have assessed the combustion effect on a free-piston engine for high performance. Kim et al. [31] and Mikalsen et al. have implemented precision piston control using PID [32] and PDF [33] (Pseudo Derivative Feedback) controllers, respectively, to control the engine speed and studied the cycle-to-cycle variation in the combustion process. Studies on the effect of varying engine stroke length and compression ratio found fewer advantages in free-piston engine performance [34].

Another aspect of engine model improvement could be the effect of the heat transfer coefficient, although, arguably, the existing heat transfer correlations are the only viable solution for automotive four-stroke engines, but not for the upcoming two-stroke engine. Dabbaghi et al. [2] studied the effect of different heat transfer correlations to predict the in-cylinder pressure and temperature. They concluded that Anand and Hohenberg's heat transfer correlation has better predictions than Woschni and Sitkei's heat transfer correction in their engine configuration. A new heat transfer model accounting for tumble motion was predicted in a two-stroke HSDI diesel engine and the results were compared with the Woschni model to confirm improvements of up to 70% in RMSE, as depicted in [35]. Hou et al. [36] have studied the effect of heat transfer on the ideal air standard cycle by considering the heat loss during the cycle of a real engine and have shown improved engine performance over a diesel engine. In the engine simulation, a highly accurate heat transfer coefficient must be used in the exhaust system to predict engine performance. This led to a proposal of a new heat model by considering the turbulence decay and velocity fluctuations, and results on enhanced predictions in engine performance are presented in [37]. A two-zone combustion model for an SI engine's heat transfer correlations is evaluated by Lounici et al. [38], considering heat loss to the chamber and heat exchange during knocking for better predictability. A multi-zone thermodynamic model for SI engine model prediction is assessed by considering flame wrinkling, flame development, geometry, and heat transfer for accurately modeling the engine combustion process [39]. The same has been reassessed by Illán et al. [40], who have shown CFD comparisons for high accuracy. Descieux et al. [41] have performed studies for thermodynamic performance improvement of a diesel engine, considering heat transfer and friction loss, and showed power and efficiency improvement. Using heat release of combustion data, a calibrated heat transfer correlation has been assessed by Guezennec et al. [42] for enhanced model prediction. The effects of heat transfer are studied not only on combustion engines, but also on sustainable mobilities such as battery electric vehicles. A numerical review of lithium-ion batteries is presented in [43], studying the effects of heat transfer for thermal runaway. The effect of heat transfer in a Stirling engine is studied for waste heat energy recovery by Catapano et al. [44]. Reliable conjugate heat transfer methodology to reduce the effect of engine heat losses is depicted in [45]. To reduce the heat transfer losses and increase thermal efficiency, an in-cylinder thermal barrier coating technique is studied by Yan et al. [46].

The novelty of this work lies in evaluating the effect of the heat transfer coefficient during scavenging to predict the in-cylinder temperature and trapped mass in an advanced two-stroke powertrain. This evaluation assesses state-of-the-art heat transfer correlations and a proposed heat transfer coefficient. The proposed heat transfer correlation uses mass flow in the intake and exhaust ports to calculate the necessary convective coefficient during scavenging, and eliminates the usage of the mean piston velocity for calculating the convective heat transfer coefficient. The methodology followed in developing the proposed heat transfer model is yet to considered in any previous state-of-the-art heat transfer correlations. All the convective models are developed in a 1D engine model, and results for the evaluation are compared with CFD simulation results. Firstly, taking advantage of the experimental campaign, the 1D model is validated for fluid-dynamic

performance. Results from the validated 1D model are then used as initial and boundary conditions for CFD simulation. Finally, the proposed heat transfer correlation results are evaluated for potential impact during scavenging. A detailed description of the procedure followed to capture the experimental results is provided in Section 2 of this manuscript. The same section shows the information on the model developed in 1D mode, validation of the 1D model, and CFD setup. Section 3 presents the method followed in developing the state-of-the-art and proposed heat transfer models. Results comparing different heat transfer models are presented and discussed in Section 4. Finally, the conclusions showing the primary outcomes of this study are outlined.

2. Materials

2.1. Experimental Setup

A prototype two-stroke advanced engine is used in this study. This engine has a notably different intake port mechanism, as depicted in Figure 1. As can be observed from Figure 1, the fresh intake charge takes place from a reed valve into an air pump and through the intake ports placed on the rod. The intake ports are a series of slots opening into the combustion chamber. Furthermore, the exhaust ports open perpendicular to the intake ports, making the fluid flow as an opposed scavenging engine. Both air pump displacement and port opening are a function of the piston position. A detailed description of the control of the engine is described in the 1D modeling subsection.

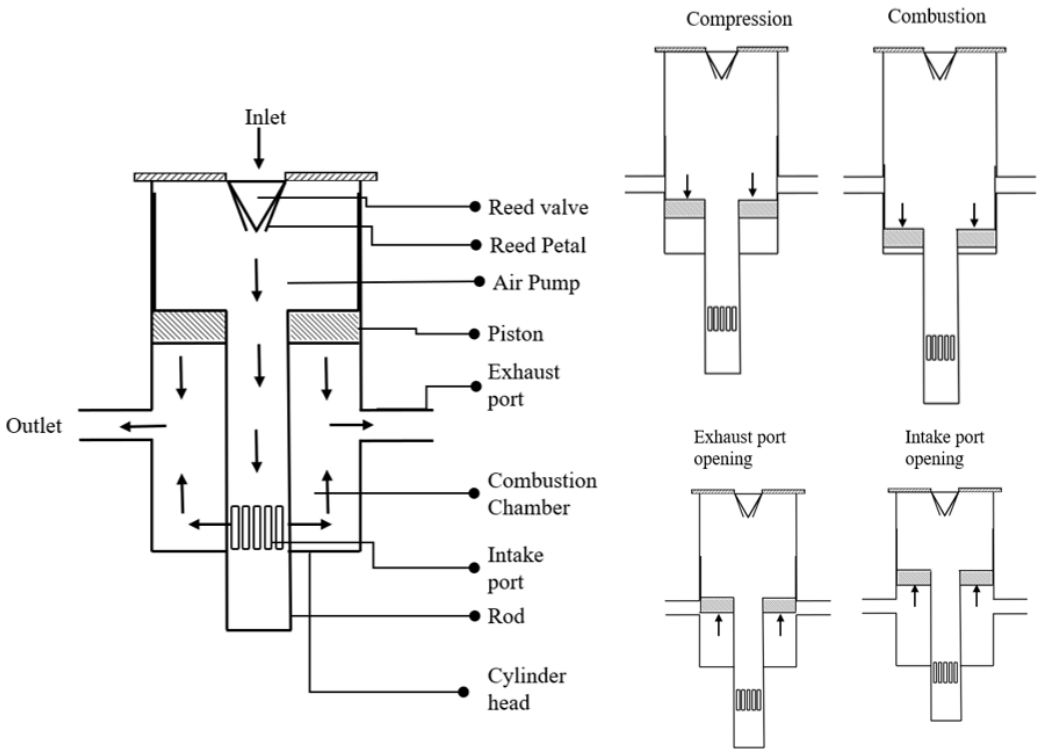

Figure 1. Schematic layout of the engine and working principle.

Several sensors capture the necessary data to assess the flow properties inside the engine. This information includes instantaneous pressure readings in the air pump, combustion chamber, and exhaust manifold. Instantaneous volume readings in the air pump, combustion chamber, and piston position are also captured. Moreover, cycled average intake air mass flow rate readings, injected fuel, throttle position, and engine speed are also captured. Other information, such as torque, power, oil temperatures, and parameters used to assess the engine performance, is also gathered. Engine tests are conducted at 2000, 2250, and 2500 rpm at full load, and partial load only at 2000 rpm. These tests also include different exhaust systems, as shown in Table 1.

Table 1. Exhaust manifold configuration at different speeds and load conditions.

Exhaust Layout	Pipe Details (mm)	Speed (rpm)	Load
Config 1	1. Exhaust manifold with tapered tailpipe 2. Long Pipe−1 (380 × 33.5) 3. Silencer (180 × 35) 4. Long Pipe−2 (650 × 33.5)	2500	Full Load
		2250	Full Load
Config 2	1. Exhaust manifold with tapered tailpipe 2. Long Pipe−1 (274.5 × 35) 3. Silencer (280 × 109)−2 units 4. "U" Pipe (213 × 35) 5. Long Pipe−2 (385 × 35)	2000	Full Load
			Partial Load

2.2. 1D Modelling

The model used for the application is developed using Virtual Engine Model (VEMOD) [47], internal software developed at CMT-Motores Térmicos, for visualizing the engine performance. The software groups elements as 0D or 1D elements depending on the spatial dimensions. In 0D elements, all the properties inside the element are constant, while in 1D elements, thermofluid dynamic properties vary with the length of the element. These 1D elements are used as intake and exhaust lines, and when the length-to-diameter ratio is high enough, the flow inside the element is fully developed. So, the most important axis for the flow movement is the X-axis—significantly reducing the calculation time, as the Y and Z axes are not relevant. This led to the proposal of a hyperbolic system of partial differential equations of simplified 1D Euler equations for unsteady compressible non-homentropic flow [47]. The software is assessed for several engine models, and results are compared with experimental data to validate the model. The results for its accurate prediction can be observed in [48]. The engine model, in addition to the pipes, also includes connections, valves, cylinders, and plenums. These elements are used for modeling the novel engine with a 0D–1D approach. The developed model uses design data for its geometry and experimental results to validate engine performance, as will be described in the model validation sub-section.

Figure 1 gives information on the major details of the engine. The major parts are the reed valve, air pump, exhaust, intake ports, and main engine block consisting of a piston and combustion chamber. The engine block developed in the model assessment uses an opposed two-stroke engine, whose cylinder is considered as a 0D element. The piston position is set by comparing the volume of the combustion chamber with experimental results. Each major element is controlled by a sub-model considering the piston position. These include the air pump volume, and the opening and closing of intake and exhaust ports. Several sensors capture necessary information on mass flow rate, volume, pressure, and temperature inside the cylinder and pipes. The information gathered is then used to develop the sub-systems for control of piston position, air pump volume, port openings and closings, and reed valve petal opening. The modeling details of the sub-systems are as follows. A discharge coefficient is used for the intake and exhaust port openings and closings, and is a function of the piston position. The discharge coefficient of the ports is calibrated to attain the instantaneous mass flow rates obtained in the CFD simulations.

From Figure 1, it can be seen that the volume of the air pump changes with the piston position. For this reason, the air pump is modeled as a variable volume. The reed valve petal is assumed to be a punctual mass concentrated in the petal tip. The lift follows the classical mass-spring-damper model, where the external force depends on the pressure difference upstream and downstream of the valve. The force balance equation is used to deduce the tip lift given by:

$$F = m\ddot{x} - b\,\dot{x} - kx, \quad (1)$$

where x is the petal tip lift, k is the spring constant, m is the petal mass, b is the damper coefficient, and F is the external force calculated with:

$$F = (p_{air\ pump} - p_{upreed}).A_{Petal}, \quad (2)$$

where A_{Petal} is the area of the petal, $p_{air\ pump}$ is the pressure downstream of the reed valve, and p_{upreed} is the pressure upstream of the reed valve. Once the petal lift is obtained, a discharge coefficient is calculated and used in the next simulation time.

2.3. Model Validation

Figure 2 depicts the information related to the 1D modeling results compared to experimental data. In Figure 2, the plot's title gives the information on the engine speed in rpm, load condition—Full Load (FL)/Partial Load (PL)—and the last digit 1 or 2 is the exhaust configuration, which is either config-1 or config-2, respectively. The results plotted in Figure 2A–D are the instantaneous pressure traces in the exhaust manifold, while Figure 2E–H depict pressure traces inside the cylinder during the scavenging process. The results only illustrate the information while the exhaust ports are open because the gas exchange occurs during this process and defines the trapped mass in the cylinder for the next engine cycle.

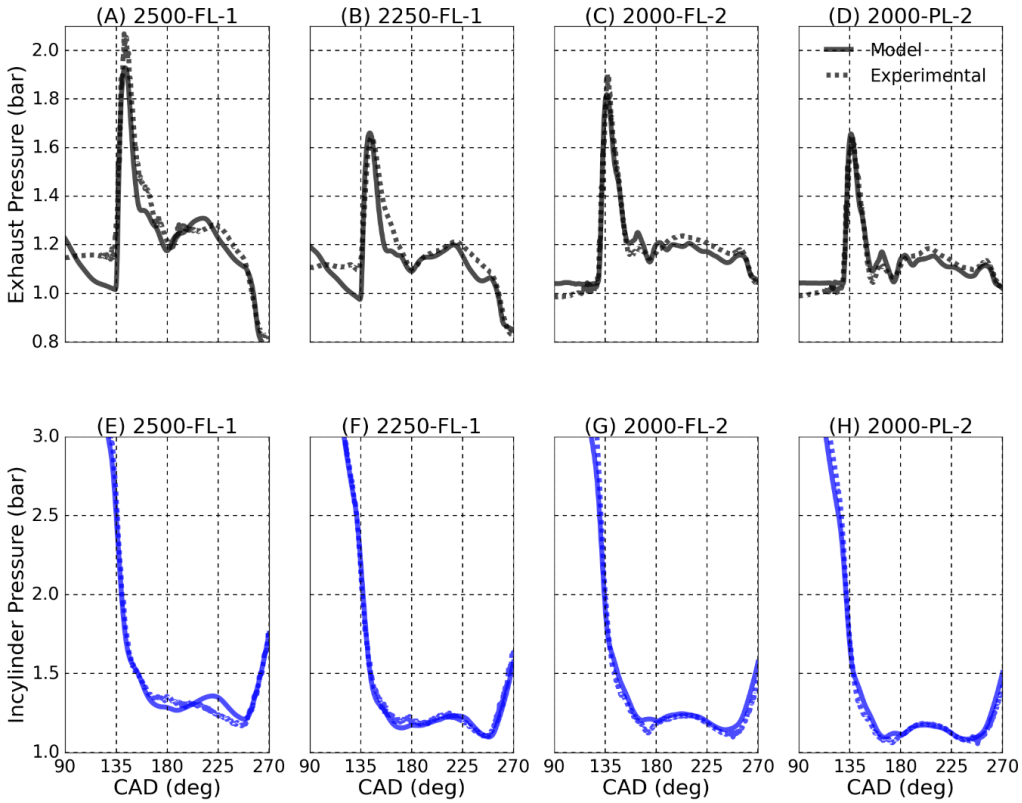

Figure 2. Comparison between experimental and 1D modeling results: CAD vs. (**A**–**D**) Exhaust pressure; (**E**–**H**) In-cylinder pressure.

Firstly, from Figure 2E–H, it can be observed that the exhaust port opening occurs at 130 CAD. The results depicted before the exhaust port opening is the expansion process, where it can be observed that the modeling results follow experimental results closely. Also, it can be observed that the port closing occurs approximately at 255 CAD and the process after this CAD is the compression stroke. During this process, it can be seen that the 1D model accurately predicts the compression stroke's pressure compared to experimental results. The process between CAD 130 and 255 is the scavenging process, where the modeling pressure traces follow the experimental measurements with an absolute

maximum deviation of less than 2%. Observing the results, it can be justified that modeling strategies employed in developing this novel engine provide accurate results during the expansion, scavenging, and compression strokes in the combustion chamber.

Secondly, as mentioned earlier, during the experimental campaign, different exhaust manifolds were employed and tested at both full load and partial load conditions; this has also been accounted for during the modeling stage. To achieve coherence between experimental results and the 1D model predictions, heat transfer and friction multipliers in the exhaust manifold were calibrated. Once a peak deviation of less than 2% was accomplished, these multipliers were held constant, and simulations were analyzed with different engine speeds and load conditions. Figure 2A–D shows that the model is calibrated to predict experimental peaks and trends accurately. Figure 2 justifies that the model provides fluid dynamically stable results to a satisfactory level and can be used for further perspective analysis, and that the results can be used as initial and boundary conditions for CFD.

2.4. 3D CFD Model

A commercial Computational Fluid Dynamics (CFD) code, CONVERGE v.2.4.33 [49], was used to implement the numerical model of the cylinder. A summary of the main features of the numerical model is shown in Table 2. The most relevant physical models, numerical schemes, and mesh details are presented here. The basis of the model has been widely described in previous investigations [50].

Table 2. CFD model setup.

Mesh Details	
Base size	4 mm
Cell size intake/exhaust ports	2 mm
Combustion chamber size	1 mm
Walls refinement	0.5 mm
Minimum cell size by AMR	0.25 mm
Numerical schemes	
Spatial discretization	The second-order central difference scheme
Temporal discretization	The first-order central difference scheme
Momentum equation correction	PISO algorithm [51]
Physical models	
Turbulence	URANS RNG k-e [52]
Heat transfer	O'Rourke and Amsden [53]

The computational domain obtained from the sketch of Figure 1 was meshed using a modified cut-cell Cartesian method directly in runtime. The base grid mesh (4 mm) was reduced in those regions where flow features have higher complexity. For instance, intake/exhaust ports were refined to 2 mm in cell size. Moreover, an adaptive mesh refinement (AMR) strategy was considered to increase the grid resolution in those regions where the sub-grid field is more prominent. The AMR cell size decreases to 0.25 mm when the sub-grid scale of velocity exceeds 1 m/s. A second-order central difference scheme was considered for spatial discretization, and a first-order scheme was considered for temporal discretization. The pressure-velocity coupling was solved by a modified Pressure Implicit with a Splitting of Operators (PISO) algorithm [54]. The in-cylinder turbulence was modeled in the frame of unsteady Reynolds-averaged Navier–Stokes (URANS) with the eddy-viscosity-based two-equation turbulence model (RNG k-ε model), used widely in ICE applications [53].

Regarding the boundary conditions, the piston, liner, and cylinder head wall temperatures were estimated from the experiments by a lumped thermal model. All instantaneous

signals at the intake/exhaust manifolds were obtained from the 1D model described in the previous section and provided as inflow/outflow boundary conditions. The wall heat transfer was estimated by the O'Rourke and Amsden model [55]. This approach is suitable for those simulations in which the turbulent boundary layer resolution is insufficient (i.e., in ICE simulations where the viscous sub-layer is not strictly resolved). The model calculates the wall heat-transfer from

$$K\frac{\partial T}{\partial x_i} = \frac{\mu_m c_p F\left(T_f - T_w\right)}{Pr_m y} n_i, \tag{3}$$

$$F = \begin{cases} 1.0 \; y' < 11.05 \\ \frac{\left(\frac{y' Pr_m}{Pr_t}\right)}{\frac{1}{k} ln(y') + B + 11.05\left(\frac{Pr_m}{Pr_t} - 1\right)} \; y' > 11.05, \end{cases} \tag{4}$$

$$y' = \frac{\rho u_\tau y}{\mu_m}, \tag{5}$$

where k is the molecular conductivity, Pr_m is the molecular Prandtl number, Pr_t is the turbulent Prandtl number, T_f is the fluid temperature, T_w is the temperature of the wall, u_τ is the shear speed, k is the Von Karman constant (0.4187), and B is a constant that depends on the turbulence model.

The convective heat transfer in fluid during scavenging is calculated using the above model to predict the heat transfer coefficient. This heat transfer coefficient will be used in subsequent studies.

3. Methods

Of the total energy produced, heat transfer represents a major energy loss that is passed to the engine coolant. Of the total heat transfer energy, more than 50% comes from in-cylinder and the rest mostly from exhaust ports. Two types of heat transfer occur in the conventional SI and CI engine: one due to convection and the other due to radiation. Most heat transfer in SI engines depends on convection, while the heat transfer due to radiation is limited to a maximum of 20%. On the contrary, in CI engines, most heat transfer is due to radiation; studies have shown that the radiative heat transfer for CI engines can reach up to 40% [49]. A most general heat transfer correlation considering the convective heat transfer correlation is given in Equation (6), where h_g is the convective heat transfer coefficient, A is the area exposed, which is the combustion chamber surface, and T_g and T_W are the gas and wall temperature, respectively:

$$\dot{Q} = h_g A\left(T_g - T_w\right). \tag{6}$$

Nevertheless, over the years, as mentioned earlier, several researchers have investigated different heat transfer correlations. The correlations investigated used the mean piston velocity to calculate the instantaneous heat transfer coefficient for CI engines and were also usable for SI engines. Convection models used for this assessment are described below.

3.1. Woschni Correlation

Woschni correlation is the most commonly applied heat transfer relation for both diesel and SI engines, and the expression is given in Equation (7) [56]:

$$h_g = aC_0 B^{-0.2} p^{0.8} w^{0.8} T^{-0.53}, \tag{7}$$

where B demotes the cylinder bore, p and T are the instantaneous pressure and temperature in the cylinder, respectively, and a is the correction multiplier. The constant C_0 is in the range of 110–130. From Equation (7), it can be deduced that the heat transfer coefficient

will behave similarly to the in-cylinder pressure evolution, with some adjustments given by the other parameters. Furthermore, w is the Woschni correlation given by Equation (8):

$$w(\theta) = C_1 \overline{U}_p + C_2 \frac{V_d T_r}{p_r V_r}(p(\theta) - p_m), \tag{8}$$

where $\overline{U}_p$ is the mean piston velocity, V_r is the reference volume, and p_r and T_r are the reference pressure and temperature. The pressure, temperature, and volume can be considered at the start of combustion or when the inlet valve closing occurs. Finally, p is the instantaneous pressure inside the cylinder with respect to the crank angle (θ), and p_m is a function of reference pressure and instantaneous in-cylinder volume given by:

$$p_{m=} p_r \left(\frac{V_r}{V}\right)^n. \tag{9}$$

The constants C_1 and C_2 depend on the piston phase, and Table 3 provides information on the calibrated values for these constants.

Table 3. Woschni correlation constants.

Phase	C_1[-]	$C_2[\frac{m}{sK}]$
Intake	6.18	0
Compression	2.28	0
Combustion	2.28	3.24×10^{-3}
Expansion	2.28	3.24×10^{-3}
Exhaust	6.18	0

3.2. Hohenberg's Correlation

Woschni correlation provides a higher averaged heat transfer coefficient during the cycle due to his approximation. Hohenberg found flaws in the results from the Woschni correlation, and created a new correlation for calculating instantaneous heat transfer by using Equation (10):

$$h_g = C_1 {V_c}^{-0.06} p^{0.8} T^{-0.4} (C_2 + \overline{U}_p), \tag{10}$$

where V_c is the cylinder volume, and p and T are the respective pressure and temperature in the combustion chamber. The constants for C_1 and C_2 obtained by Hohenberg were precisely measured for diesel engines by heat balance, heat flux, and combustion chamber temperatures. The values are kept constant at 130 and 1.4, respectively. He has demonstrated that his correlation could predict temperatures with an accuracy of 10% marginal error [57].

3.3. Anand Correlation

Anand predicted the instantaneous heat transfer coefficient using Nusselt and Reynolds non-dimensional numbers [58]. His correlation considers both convection and radiative heat transfer coefficients. As for this engine application, radiative heat transfer is not used. Therefore, the correlation only considers the convective heat transfer coefficient and is given in Equation (11):

$$h_g = \frac{d k_{gas} Re^{0.7}}{B}, \tag{11}$$

where Re is the Reynolds number, B is the bore diameter, and k_{gas} is the thermal conductivity of the gas, which can be deduced from experimental polynomial curve fitting using the working temperature of the fluid. The coefficient d is the correction coefficient given by Anand using Sieder-Tate given in Equation (12) [59]:

$$d = 0.023 Pr^{0.4}, \tag{12}$$

where Pr is the Prandtl number. Furthermore, the flow velocity used in the Reynolds number calculation is the mean piston velocity.

The correlations mentioned above are established based on four-stroke diesel engine experiments. Due to the differences in the combustion principles between SI and CI engines, practically, these models cannot provide a viable solution but can be considered for SI engines as well. As mentioned earlier, several researchers have theoretically and practically shown that, with minor adjustments, the above correlations can also be used for SI engines.

3.4. Proposed Heat Transfer Correlation

The proposed model uses the velocity of the air mass flow calculated using instantaneous mass flows during the intake and exhaust port openings and closings, which has yet to be accounted for in any heat transfer model described previously. An average pseudo-mass flow rate inside the cylinder is expressed in Equation (13):

$$\dot{m}^* = \left| \frac{\dot{m}_{in} + \dot{m}_{out}}{2} \right|, \tag{13}$$

where $\dot{m}_{in}$ and $\dot{m}_{out}$ are the intake and exhaust mass flow rates, respectively. Furthermore, by using Equation (14), the pseudo-velocity variable is defined, which is an approximation for the averaged velocity field inside the cylinder (c^*), which is calculated as:

$$c^* = \frac{\dot{m}^*}{A\,\rho}, \tag{14}$$

In which A is the area of the piston and ρ is the density of the gases calculated using the instantaneous pressure and temperature in the cylinder. Using the velocity, the non-dimensional Reynolds number (Re) is calculated with:

$$Re = \frac{Dc^*\rho}{\mu}, \tag{15}$$

where D is the diameter of the combustion chamber and μ is the fluid's dynamic viscosity. Using the correlation between the Reynolds and Nusselt numbers (Nu), Nu is calculated using Equation (16):

$$Nu = bRe^{0.7}, \tag{16}$$

where b is the correction coefficient. It is also known that Nu is a function of the convective heat transfer coefficient (h_{ins}), a spatial dimension; in this case, the diameter of the combustion chamber (D) is used, and the thermal gases conductivity (k). The appropriate heat transfer coefficient is calculated using this correlation in Equation (17):

$$h_{ins} = \frac{Nu\,k}{D}. \tag{17}$$

Figure 3 depicts information on the convective heat transfer coefficient calculations adapted for this engine during scavenging in conjunction with the Woschni heat transfer coefficient calculated during combustion. The results plotted in Figure 3A depict mass flow rates in the intake and the exhaust ports. Figure 3B depicts the average mass flow rate calculated using Equation (13). Using Equations (14)–(17), the convective heat transfer coefficient results during scavenging are calculated and plotted using a solid red line, as depicted in Figure 3C. In contrast, a solid blue line depicting Woschni's heat transfer coefficient calculated using Equation (7) is plotted in Figure 3C. The actual convective heat transfer coefficient actuated in the cylinder is plotted in Figure 3D. A min/max control objective is used to actuate the switch between the Woschni heat transfer coefficient during combustion and the proposed transfer model during scavenging. From Figure 3C,D, it can be observed that the blue investigation window marked as 'a' during scavenging is initiated at the moment when the exhaust port opens and lasts until the exhaust ports

close. In contrast, the Woschni convective coefficients are actuated during the compression, combustion, and expansion strokes.

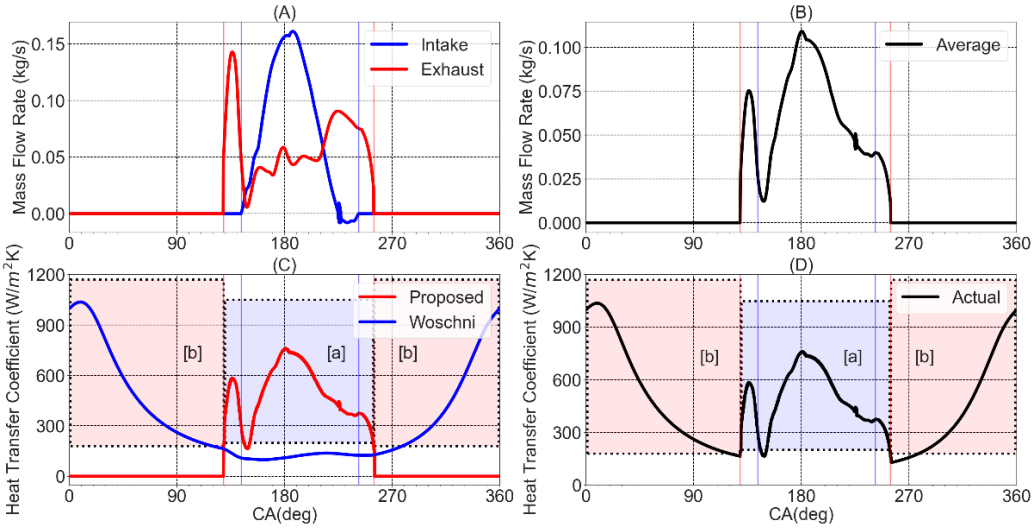

Figure 3. (**A**): Mass flow rate at intake and exhaust pipes, (**B**): Average mass flow rate, (**C**): Convective heat transfer for proposed and Woschni models, (**D**): Actual convective heat transfer of overall cycle.

4. Results and Discussion

In this study, the simulations are analyzed under three conditions. Firstly, a reliability study is performed where heat transfer models are subject to identical initial conditions to CFD simulations. By doing such an operation, the robustness of the proposed heat transfer model is shown to capture in-cylinder temperature and trapped mass. Secondly, only Woschni and the proposed heat transfer models are studied to evaluate the impact on engine performance, in which combustion and heat transfer settings are restrained. Finally, a sensitivity analysis depicting the impact of the correction coefficients of the correlations is studied.

4.1. Reliability Assessment of Heat Transfer Models

As mentioned earlier, the effect of different heat transfer correlations is studied, including Anand, Hohenberg, Woschni, and the proposed heat transfer model developed for uniflow scavenged two-stroke engines. This study uses the information from the experimentally validated model at 2250 rpm with a Config-1 exhaust manifold. All the heat transfer correlations are validated for the same initial conditions at the exhaust port opening, as depicted in Figure 4.

The information in Figure 4 shows that the fluid behavior for all heat transfer correlations, compared to CFD, is similar. These include the peaks and trends in the intake mass flow rate-Figure 4A, exhaust mass flow rate-Figure 4B, pressure in the cylinder-Figure 4C, and pressure in the exhaust manifold-Figure 4D during the scavenging process. At the same time, comparing results with the 1D model, Figure 4C not only shows the information of the 1D model to CFD comparison but also provides the information with experimental in-cylinder pressure traces. This validates the 1D model compared to experimental results and the CFD simulation predictability of experimental results.

The study focuses on the effect due to heat transfer in predicting the in-cylinder temperature. For such studies, not only are the fluid parameters, such as pressure and mass flows in the intake and exhaust, needed for validation, but also the thermal parameter needs to be equal. For this reason, the temperature values at the exhaust port opening need to be identical to those observed in CFD simulations. This was achieved by calibrating the correction coefficient of each correlation. Maintaining identical initial conditions in in-cylinder pressure and temperature ensured that the trapped mass at the exhaust port opening would be constant. The information on similar thermal boundary conditions and trapped mass is provided in Figure 5.

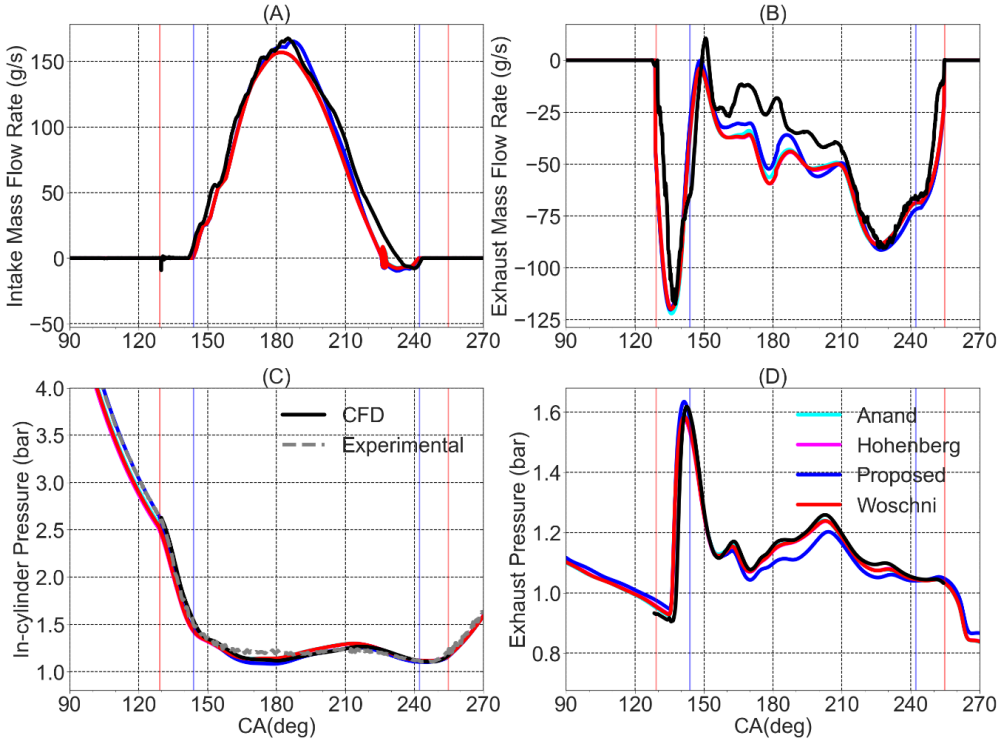

Figure 4. 1D model to CFD comparison for different heat transfer coefficients. (**A**): Intake mass flow rate, (**B**): Exhaust mass flow rate, (**C**): In-cylinder pressure during scavenging process, (**D**): Exhaust manifold pressure.

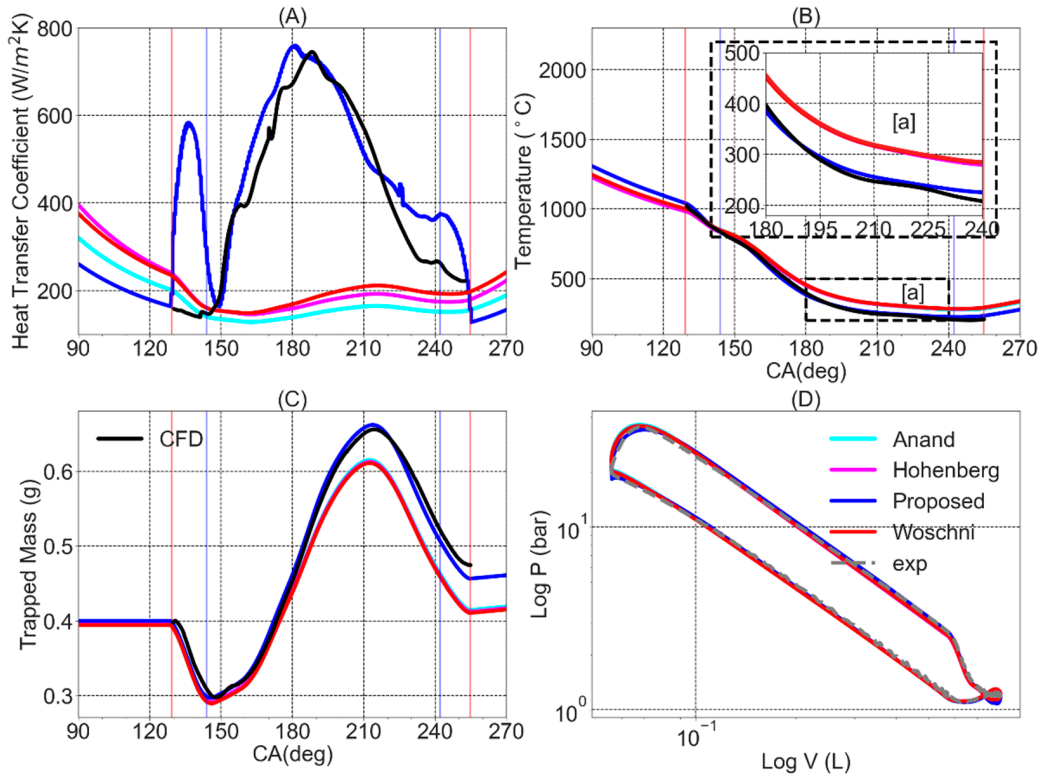

Figure 5. 1D model vs. CFD comparison of (**A**): Heat transfer coefficient (**B**): Temperature, (**C**): In-cylinder trapped mass, (**D**): Experimental vs. 1D simulation results comparison for logarithm pressure vs. Volume evolution.

Figure 5A provides information on the heat transfer coefficient used in this study during the scavenging process. A solid black line depicting the instantaneous heat transfer coefficient from CFD simulation is depicted in Figure 5A. It can be seen from Figure 5A that the methodology followed in developing the proposed heat transfer provides similar peaks and follows trends as in CFD simulations during scavenging. On the other hand, the state-of-the-art heat transfer correlations fail to provide the necessary heat transfer coefficient during the same process. Figure 5B provides the information with temperature traces achieved due to the adjusted heat transfer coefficient. Figure 5C depicts the information on the trapped mass inside the cylinder during scavenging. Figure 5B,C show CFD results plotted with a solid black line, showing the temperature and trapped mass, respectively, which are the same as in the 1D model at the opening of the exhaust ports. Figure 5D provides information (in logarithmic scales) related to evolution inside the combustion chamber for the 1D model and experimental data. Figure 5D results justify that the combustion settings used in the modeling stage provide accurate results. Observing the trends and patterns from Figures 4 and 5, it can be justified that comparing different heat transfer models is viable as all models have similar behavior.

On observing the instantaneous temperature traces in the zoomed area 'a' in Figure 5B, it can be seen that the classical heat transfer correlations based on the Reynolds number calculated with the mean piston speed predict higher temperature during scavenging compared with CFD results. Due to the lack of temperature predictability during scavenging, the state-of-the-art correlations also fail to reproduce the trapped mass in the cylinder while comparing results with CFD, as shown in Figure 5C when the exhaust ports close (around 255 CAD). On the other hand, the proposed heat transfer model developed considering the pseudo-velocity inside the cylinder accurately captures the temperature and trapped mass calculated by CFD. To quantify the results for trapped mass and temperature, readings for the same are captured at specific moments and presented in Table 4. The four instances are: at the exhaust port opening (130 CAD), intermediate positions (170 and 210 CAD), and finally, at the exhaust port closing (255 CAD). Moreover, since Anand, Hohenberg, and Woschni's heat transfer coefficients provide similar outputs, only results from Woschni are used for further comparisons. Using Equations (18) and (19), differences in CFD and 1D modeling results are provided in Table 4 for in-cylinder trapped mass and temperature, respectively.

$$Error(\%) = \left(\frac{CFD - Model}{CFD}\right) \times 100, \tag{18}$$

$$Error(^{\circ}\mathrm{C}) = CFD - Model. \tag{19}$$

Table 4. Comparison of CFD vs. 1D modeling results of different correlations at 130, 170, 210, and 255 CAD for in-cylinder mass and temperature.

Crank Angle [°]	Trapped Mass [g]			Temperature [°C]		
	CFD	Proposed (Error %)	Woschni (Error %)	CFD	Proposed (Error °C)	Woschni (Error °C)
130	0.39	0.39 (0)	0.39 (0)	1015	1024 (−9)	1000 (15)
170	0.37	0.38 (−2.7)	0.36 (2.7)	519	511 (7)	564 (−46)
210	0.65	0.65 (0)	0.60 (7.69)	246	255 (−9)	319 (−73)
255	0.48	0.47 (2.08)	0.42 (12.5)	201	226 (−25)	285 (−84)

Since the initial conditions at the exhaust port opening for CFD and heat transfer models are very similar, no significant differences are found in either trapped mass or temperature. At 170 CAD, the proposed and Woschni heat transfer correlations show a trapped mass of 0.38 and 0.36 g, respectively. These results are almost the same, as CFD simulations depict a trapped mass of 0.37 g. Contrarily, the temperature predictions using the Woschni correlation show an absolute deviation of 46 °C. This deviation in temperature is due to the lower convective heat transfer coefficient, which according to the calculation, provides 230 $\frac{W}{m^2K}$.

On the other hand, the proposed heat transfer correlation calculation provides a convective coefficient of approximately 800 $\frac{W}{m^2K}$. This coefficient value leads to a lower temperature prediction of 511.8 °C, which is 7 °C lower than the CFD result of 519 °C. The lack of higher convective coefficients using the Woschni heat transfer correlation led to lower heat dissipation and increased fluid temperature inside the cylinder. These deviations in temperature prediction using the Woschni heat transfer coefficient are even higher at 210 and 255 CAD, where a deviation of 72.3 °C and 84.4 °C, respectively, can be observed. Due to higher temperature predictions, lower trapped mass can be observed for Woschni heat transfer calculations. About 7% lower trapped mass can be observed at 210 CAD, while a 12.5% lower trapped mass can be seen at 255 CAD. All these deviations are attributed to a lack of proper heat transfer coefficients.

On the other hand, the temperature and trapped mass errors are lower using the proposed heat transfer model, which accounts for the high flow velocity inside the cylinder during the scavenging process and better approaches the CFD results. Due to this, the fluid inside the cylinder is adequately cooled, and lower fluid temperatures are seen. The proposed heat transfer model predicts about 64 °C lower temperature while comparing results with Woschni (at 210 CAD). This led to an accurate prediction of trapped mass at 210 CAD, although, at 255 CAD, CFD results depict about 201 °C, and the proposed model provides a 25 °C higher temperature but accurately predicts the trapped mass. Finally, observing trends in Figure 5B,C and Table 4, it can be said that the proposed heat transfer model accurately predicts the temperature and trapped mass by employing a higher convective coefficient compared with state-of-the-art models.

4.2. Performance Assessment of Heat Transfer Models

In this study, the heat transfer correlations (Woschni and proposed) are assessed under similar combustion settings to evaluate the potential of the proposed heat transfer model. To meet the objectives of the current study, the combustion duration is set to 45 CAD, and the start of combustion at 11 CAD before TDC, while maintaining a constant air-to-fuel ratio of 14.7. Along with the combustion parameters, the peak of the heat transfer coefficient during combustion (Woschni and proposed) and scavenging in the proposed heat transfer model is set to the value of 2100 W/m^2k, as depicted in Figure 6A. This has been done by calibrating the coefficient b in Equation (16). Moreover, the engine speed and exhaust configuration are the same as in the previous study.

As from the previous study, it is well established that a higher heat transfer coefficient leads to a lower in-cylinder fluid temperature. Similar results on lower fluid temperature using the proposed heat transfer coefficient over the Woschni correlation can be observed from Figure 6B. This led to higher trapped mass using the proposed heat transfer model, as depicted in Figure 6C. Two quantifiable results can be seen in this evaluation: one during scavenging, i.e., temperature profiles and their impact on the trapped mass; the other is the effect on the combustion pressure due to higher trapped mass, which can be seen in Figure 6D. Quantifying results during scavenging, the results on the instantaneous heat transfer coefficient during scavenging show that the Woschni heat transfer coefficient is as low as 200 W/m^2k (data captured at 210 CAD). While for the same piston position, the proposed heat transfer model provides a peak coefficient of 2100 W/m^2k, leading to 80 °C lower temperature, as depicted in the zoom area 'a' in Figure 6B. Due to this lower fluid temperature, a peak trapped mass of 0.68 g can be seen using the proposed heat transfer

correlation. On the other hand, the Woschni correlation depicts a peak trapped mass of 0.62 g, which is approximately 9% lower in trapped mass.

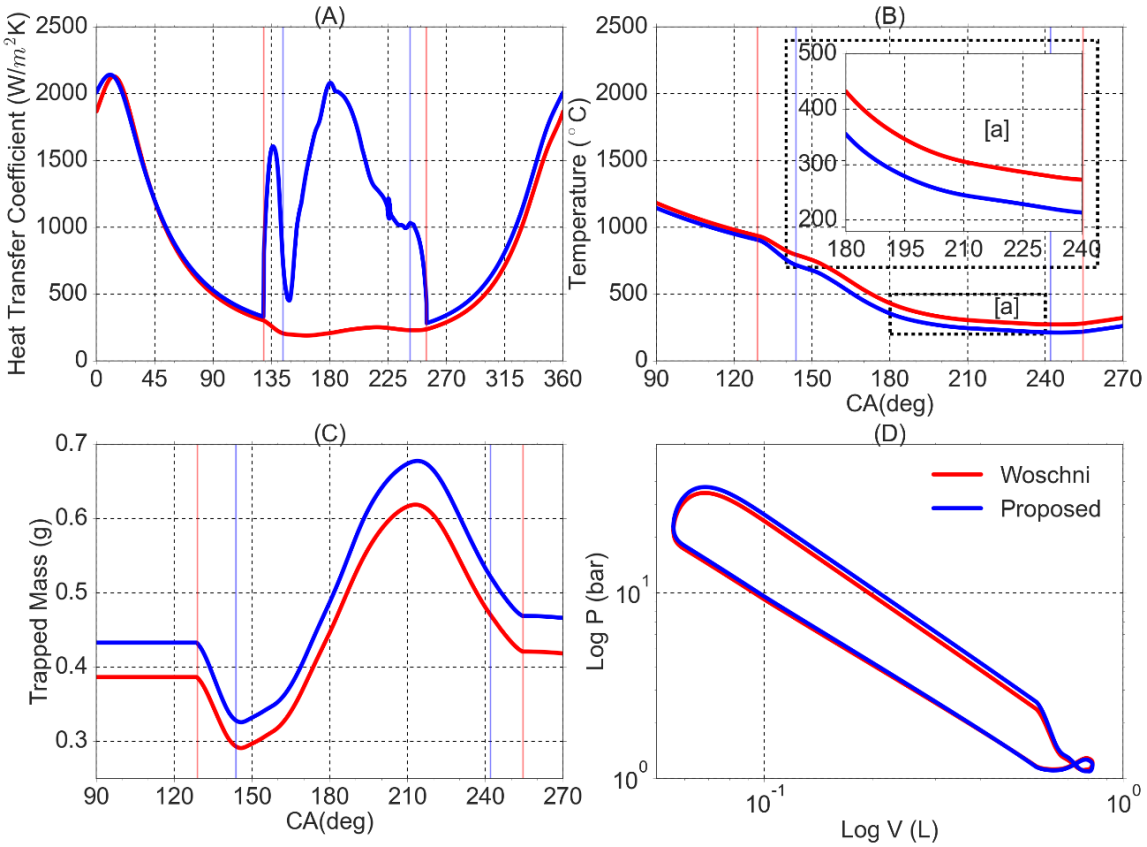

Figure 6. Results comparing Woschni and proposed heat transfer model for (**A**): Heat transfer coefficient-1D model (**B**): In-cylinder temperature evolution during scavenging, (**C**): In-cylinder trapped mass, (**D**): logarithm pressure vs. Volume evolution.

Due to the above phenomena, the trapped mass at the exhaust port closing is higher in the proposed model. A trapped mass of 0.48 g using the proposed model can be seen, while the state-of-the-art model depicts 0.42 g. Due to this additional trapped mass, and under similar AFR ratio and combustion settings, an increased pressure during combustion can be observed. To quantify the enhanced performance of the proposed model, the Indicated Mean Effect Pressure (*IMEP*) is used, given by:

$$IMEP = \frac{1}{V_{disp}} \int p \, dV, \tag{20}$$

where V_{disp} is the displacement volume of the cylinder, p is the pressure, and V is the volume of the cylinder. Using Equation (20), an *IMEP* of 3.49 and 3.92 bar can be observed for Woschni and the proposed heat transfer model, respectively. In other words, approximately a 12% difference in engine performance can be detected when using different heat transfer models.

4.3. Sensitivity Analysis

As mentioned earlier, the proposed heat transfer model uses a combination of Woschni heat transfer correlation during combustion and the proposed heat transfer during scavenging calculated, using Equation (7) and Equation (16), respectively. Two constants are used to adjust the correlation coefficients, one to adjust the combustion (coefficient a in the Woschni equation) and the other for the proposed heat transfer coefficient (coefficient b). A

sensitivity analysis is performed by varying the two coefficients to assess the impact on the trapped mass at the end of the scavenging process. Furthermore, in this analysis, the engine settings are maintained as in Section 4.2.

In this analysis, 35 points are studied, with values for coefficient b ranging from 2–6 and coefficient a ranging from 40–100. Figure 7A provides the information on the effect on trapped mass in absolute terms, while Figure 7B, depicts the information on the differences in trapped mass with variations in percentage in coefficients a and b from the mean values. For this calculation, Equation (21) is used:

$$c_i = \left(\frac{v_i}{\overline{v}} - 1\right) 100, \tag{21}$$

where v_i is the respective value of coefficient a, b or trapped mass and $\overline{v}$ is the mean value for coefficient a is 4, while the mean value for coefficient b is 70 and the mean value of trapped mass is approximately 0.455 g. From Figure 7, it can be observed that the effect of coefficient b has a higher impact on trapped mass than coefficient a.

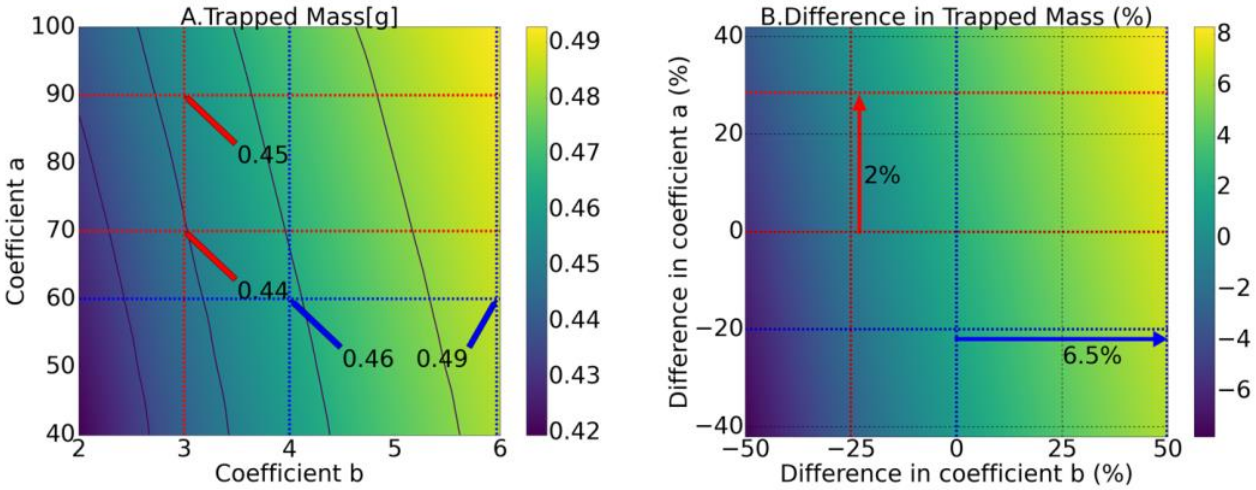

Figure 7. (**A**): Effect on trapped mass varying coefficients a and b and (**B**): Difference in trapped mass (%) varying differences in coefficients a and b (%).

For instance, from Figure 7A, considering a horizontal line at coefficient a of 60 (blue dotted line) and observing the trapped mass at coefficient b of 4 yields a value of 0.46 g, while for the same value of coefficient a and a coefficient b of 6, it can be seen from Figure 7A that the trapped mass has changed to 0.49 g. This change in trapped mass is about 6.5%, as observed in Figure 7B. On the other hand, from Figure 7A, for a constant value of coefficient b of 3 (red dotted line) and changing the coefficient a from 70 to 90 results in a trapped mass of 0.44 and 0.45 g, respectively. In other words, a change of 2% in trapped mass can be observed from Figure 7B. This analysis shows that the results for trapped mass are affected by the chosen value of coefficient b, so special care has to be taken when calibrating the model correlation.

5. Conclusions

This article assessed a model-based calibration of the heat transfer coefficient during scavenging for a uniflow scavenged two-stroke engine. A 1D model, fluid-dynamically validated against experimental data, was used for this assessment. The experimental tests consisted of three engine speeds (2000, 2250, and 2500 rpm), with two different exhaust system configurations at full and partial loads conducted only at 2000 rpm. On observing satisfactory outputs for the 1D model, these results were used as initial and boundary conditions in CFD simulations to validate the scavenging process. CFD simulation results showed that the state-of-the-art heat transfer models embedded in a 1D engine model failed

to predict the in-cylinder temperature during scavenging. The temperature deviations also led to an error in predicting the trapped mass. A new heat transfer model was proposed, considering a pseudo-velocity that accounts for the flow motion inside the cylinder to calculate the Reynolds number. This calculation was based on the instantaneous mass flows in the exhaust and intake ports. The thermo-fluid dynamically validated 1D model was used for perspective analysis to showcase the potential of the heat transfer model for its robustness and performance, as follows:

- Under identical initial conditions for all the heat transfer correlations, it was observed that the state of art correlations, which include Anand, Hohenberg, and Woschni heat transfer correlations, provide similar results during scavenging. The heat transfer coefficient during scavenging can be as low as 200 $\frac{W}{m^2K}$, leading to a peak deviation of 85 °C in temperature predictions and up to 12% in deviation for trapped mass predictions. On the other hand, the proposed heat transfer model calculates a peak coefficient of 800 $\frac{W}{m^2K}$ during scavenging, leading to a peak temperature deviation of 25 °C along with almost negligible error in trapped mass predictions.
- Under identical combustion settings and a similar peak heat transfer coefficient, a difference in trapped mass of up to 6% at the exhaust port closing was observed using the proposed heat transfer model. The gases inside the cylinder were cooled a further 85 °C, leading to a higher trapped mass. This translated to differences of up to 12% in the IMEP of the engine.
- A sensitivity analysis was performed to evaluate the impact of the model constants on the engine operation. These constants included both Woschni and the proposed heat transfer correlation during scavenging. In this analysis, coefficient b (correction coefficient of proposed heat transfer correlation) was changed by $\pm$50% from the mean value, and coefficient a (correction coefficient of Woschni heat transfer correlation) was changed by $\pm$42%. Results depicted that coefficient b had a more significant impact on trapped mass. A sweep along varying coefficient b and at constant coefficient a can lead to a 15% change in trapped mass. Conversely, a sweep along varying coefficient a and at constant coefficient b can lead to a maximum difference of 5% in trapped mass.

Author Contributions: H.C.: Resources, Supervision, Project administration, Conceptualization, Writing—original draft, Writing—review & editing. A.T.: Resources, Formal analysis, Writing—original draft, Writing—review & editing. J.G.-S.: Writing—review & editing, Methodology. A.D.: Conceptualization, Methodology, Software, Validation, Formal analysis, Investigation, Writing—original draft, Writing—review & editing. All authors have read and agreed to the published version of the manuscript.

Funding: This research received no external funding.

Institutional Review Board Statement: Not applicable.

Informed Consent Statement: Not applicable.Informed Consent StatementNot applicable.

Data Availability Statement: The data that supports the findings of this study are available from the corresponding author upon reasonable request.

Conflicts of Interest: The authors declare no conflict of interest.

Abbreviations

Symbols	Nomenclature	Units
a	Correction coefficient of Woschni correlation	N/a
A	Area	m^2
b	Correction coefficient of proposed correlation	N/a
b	Damper coefficient	$\frac{Ns}{m}$
B	Bore	m
CAD, θ	Crank angle	degrees
C_0,C_1,C_2	Correction coefficients	N/a
c*	Pseudo velocity	$\frac{m}{s}$
D	Diameter	m
F	Force	Pascal
h	Convective heat transfer coefficient	$\frac{W}{m^2K}$
IMEP	Indicative mean effective pressure	bar
k	Spring constant	$\frac{N}{m}$
K_{gas}	Thermal conductivity	$\frac{W}{mK}$
m	Mass	g
$\dot{m}$	Mass flow rate	$\frac{kg}{s}$
Nu	Nusselt number	N/a
p	Pressure	Pascal
Pr	Prandtl number	N/a
$\dot{Q}$	Rate of heat transfer	$\frac{J}{s}$
Re	Reynold number	N/a
T	Temperature	K
$\overline{U}_p$	Mean piston velocity	$\frac{m}{s}$
V	Volume	m^3
x	Displacement	m
$\dot{x}$	Velocity	$\frac{m}{s}$
$\ddot{x}$	Acceleration	$\frac{m}{s^2}$
ρ	Density	$\frac{kg}{m^3}$
μ	Dynamic Viscosity	$\frac{kg}{ms}$

References

1. García-Oliver, J.M.; Novella, R.; Micó, C.; Bin-Khalid, U. A numerical investigation of the performance of oxymethylene ethers blended with fossil diesel to reduce soot emissions in compression ignition engines. *Fuel* **2022**, *324*, 124768. [CrossRef]
2. Dabbaghi, M.; Baharom, M.; Karim, Z.A.; Aziz, A.R.A.; Mohammed, S.E. Comparative evaluation of different heat transfer correlations on a single curved-cylinder spark ignition crank-rocker engine. *Alex. Eng. J.* **2021**, *60*, 2963–2978. [CrossRef]
3. Serrano, J.; Arnau, F.; Bares, P.; Gomez-Vilanova, A.; Garrido-Requena, J.; Luna-Blanca, M.; Contreras-Anguita, F. Analysis of a novel concept of 2-stroke rod-less opposed pistons engine (2S-ROPE): Testing, modelling, and forward potential. *Appl. Energy* **2021**, *282*, 116135. [CrossRef]
4. Mikalsen, R.; Roskilly, A. A computational study of free-piston diesel engine combustion. *Appl. Energy* **2009**, *86*, 1136–1143. [CrossRef]
5. Jia, B.; Smallbone, A.; Zuo, Z.; Feng, H.; Roskilly, A.P. Design and simulation of a two- or four-stroke free-piston engine generator for range extender applications. *Energy Convers. Manag.* **2016**, *111*, 289–298. [CrossRef]
6. Mikalsen, R.; Roskilly, A. A review of free-piston engine history and applications. *Appl. Therm. Eng.* **2007**, *27*, 2339–2352. [CrossRef]
7. Mikalsen, R.; Roskilly, A. Performance simulation of a spark ignited free-piston engine generator. *Appl. Therm. Eng.* **2008**, *28*, 1726–1733. [CrossRef]
8. Herold, R.; Wahl, M.; Regner, G.; Lemke, J.; Foster, D.E. *Thermodynamic Benefits of Opposed-Piston Two-Stroke Engines*; SAE Technical Paper 2011-01-2216; SAE International: Pittsburgh, PA, USA, 2011. [CrossRef]
9. Buidin, T.; Mariasiu, F. Modeling Approach of an Air-Based Battery Thermal Management System for an Electric Vehicle. *Appl. Sci.* **2021**, *11*, 7089. [CrossRef]
10. Wang, X.; Zhao, H. A High-Efficiency Two-Stroke Engine Concept: The Boosted Uniflow Scavenged Direct-Injection Gasoline (BUSDIG) Engine with Air Hybrid Operation. *Engineering* **2019**, *5*, 535–547. [CrossRef]
11. Wang, X.; Zhao, H. *Analysis of the Boost System for a High Performance 2-Stroke Boosted Uniflow Scavenged Direct Injection Gasoline (BUSDIG) Engine*; SAE Technical Paper; SAE International: Atlanta, GA, USA, 2020. [CrossRef]
12. Wang, X.; Zhao, H. Effect of piston shape design on the scavenging performance and mixture preparation in a two-stroke boosted uniflow scavenged direct injection gasoline engine. *Int. J. Engine Res.* **2020**, *22*, 1484–1499. [CrossRef]

13. Benson, R.S.; Brandham, P.T. A method for obtaining a quantitative assessment of the influence of charging efficiency on two-stroke engine performance. *Int. J. Mech. Sci.* **1969**, *11*, 303–312. [CrossRef]
14. Sakellaridis, N.F.; Raptotasios, S.I.; Antonopoulos, A.K.; Mavropoulos, G.C.; Hountalas, D.T. Development and validation of a new turbocharger simulation methodology for marine two stroke diesel engine modelling and diagnostic applications. *Energy* **2015**, *91*, 952–966. [CrossRef]
15. Zareei, J.; Kakaee, A.H. Study and the effects of ignition timing on gasoline engine performance and emissions. *Eur. Transp. Res. Rev.* **2013**, *5*, 109–116. [CrossRef]
16. Foteinos, M.I.; Papazoglou, A.; Kyrtatos, N.P.; Stamatelos, A.; Zogou, O.; Stamatellou, A.-M. A Three-Zone Scavenging Model for Large Two-Stroke Uniflow Marine Engines Using Results from CFD Scavenging Simulations. *Energies* **2019**, *12*, 1719. [CrossRef]
17. Zhu, S.; Gu, Y.; Yuan, H.; Ma, Z.; Deng, K. Thermodynamic analysis of the turbocharged marine two-stroke engine cycle with different scavenging air control technologies. *Energy* **2019**, *191*, 116533. [CrossRef]
18. Kim, J.-S.; Lee, W.-J.; Pham, V.C.; Choi, J.-H. A Numerical Study on Fuel Injection Optimization for a ME-GI Dual-Fuel Marine Engine Based on CFD Analysis. *Appl. Sci.* **2022**, *12*, 3614. [CrossRef]
19. Moreno, P.B. In-Cylinder Pressure Resonance Analysis for Trapped Mass Estimation in Automotive Engines. Ph.D. Thesis, Universitat Politècnica de València, Valencia, Spain, June 2017. [CrossRef]
20. Carlucci, A.P.; Ficarella, A.; Laforgia, D.; Longo, M. An Easy and Inexpensive Way to Estimate the Trapping Efficiency of a two Stroke Engine. *Energy Procedia* **2015**, *82*, 17–22. [CrossRef]
21. Di Leo, R. Methodologies for Air-Fuel ratio and trapped mass estimation in Diesel engines using the in-cylinder pressure measurement. *Energy Procedia* **2015**, *82*, 957–964. [CrossRef]
22. Arsie, I.; Di Leo, R.; Pianese, C.; De Cesare, M. Estimation of in-cylinder mass and AFR by cylinder pressure measurement in automotive Diesel Engines. 2014, 47, 11836–11841. *Diesel Engines* **2014**, *47*, 11836–11841. [CrossRef]
23. Jia, B.; Smallbone, A.; Feng, H.; Tian, G.; Zuo, Z.; Roskilly, A. A fast response free-piston engine generator numerical model for control applications. *Appl. Energy* **2016**, *162*, 321–329. [CrossRef]
24. Jia, B.; Zuo, Z.; Tian, G.; Feng, H.; Roskilly, A. Development and validation of a free-piston engine generator numerical model. *Energy Convers. Manag.* **2015**, *91*, 333–341. [CrossRef]
25. Jia, B.; Zuo, Z.; Feng, H.; Tian, G.; Smallbone, A.; Roskilly, A. Effect of closed-loop controlled resonance based mechanism to start free piston engine generator: Simulation and test results. *Appl. Energy* **2016**, *164*, 532–539. [CrossRef]
26. Chan, S.H.; Zhu, J. Modelling of engine in-cylinder thermodynamics under high values of ignition retard. *Int. J. Therm. Sci.* **2001**, *40*, 94–103. [CrossRef]
27. Jia, B.; Mikalsen, R.; Smallbone, A.; Zuo, Z.; Feng, H.; Roskilly, A.P. Piston motion control of a free-piston engine generator: A new approach using cascade control. *Appl. Energy* **2016**, *179*, 1166–1175. [CrossRef]
28. Li, K.; Zhang, C.; Sun, Z. Precise piston trajectory control for a free piston engine. *Control. Eng. Pract.* **2015**, *34*, 30–38. [CrossRef]
29. Feng, H.; Guo, C.; Jia, B.; Zuo, Z.; Guo, Y.; Roskilly, T. Research on the intermediate process of a free-piston linear generator from cold start-up to stable operation: Numerical model and experimental results. *Energy Convers. Manag.* **2016**, *122*, 153–164. [CrossRef]
30. Dižo, J.; Blatnický, M.; Sága, M.; Šťastniak, P. A Numerical Study of a Compressed Air Engine with Rotating Cylinders. *Appl. Sci.* **2021**, *11*, 7504. [CrossRef]
31. Kim, J.; Bae, C.; Kim, G. Simulation on the effect of the combustion parameters on the piston dynamics and engine performance using the Wiebe function in a free piston engine. *Appl. Energy* **2013**, *107*, 446–455. [CrossRef]
32. Mikalsen, R.; Roskilly, A. The control of a free-piston engine generator. Part 1: Fundamental analyses. *Appl. Energy* **2010**, *87*, 1273–1280. [CrossRef]
33. Mikalsen, R.; Roskilly, A. The control of a free-piston engine generator. Part 2: Engine dynamics and piston motion control. *Appl. Energy* **2010**, *87*, 1281–1287. [CrossRef]
34. Mikalsen, R.; Roskilly, A. The design and simulation of a two-stroke free-piston compression ignition engine for electrical power generation. *Appl. Therm. Eng.* **2008**, *28*, 589–600. [CrossRef]
35. Olmeda, P.; Martín, J.; Novella, R.; Carreño, R. An adapted heat transfer model for engines with tumble motion. *Appl. Energy* **2015**, *158*, 190–202. [CrossRef]
36. Hou, S.-S. Heat transfer effects on the performance of an air standard Dual cycle. *Energy Convers. Manag.* **2004**, *45*, 3003–3015. [CrossRef]
37. Luján, J.M.; Climent, H.; Olmeda, P.; Jiménez, V.D. Heat transfer modeling in exhaust systems of high-performance two-stroke engines. *Appl. Therm. Eng.* **2014**, *69*, 96–104. [CrossRef]
38. Lounici, M.S.; Loubar, K.; Balistrou, M.; Tazerout, M. Investigation on heat transfer evaluation for a more efficient two-zone combustion model in the case of natural gas SI engines. *Appl. Therm. Eng.* **2011**, *31*, 319–328. [CrossRef]
39. Verhelst, S.; Sheppard, C. Multi-zone thermodynamic modelling of spark-ignition engine combustion – An overview. *Energy Convers. Manag.* **2009**, *50*, 1326–1335. [CrossRef]
40. Illán, F.; Alarcón, M. Numerical analysis of combustion and transient heat transfer processes in a two-stroke SI engine. *Appl. Therm. Eng.* **2010**, *30*, 2469–2475. [CrossRef]
41. Descieux, D.; Feidt, M. One zone thermodynamic model simulation of an ignition compression engine. *Appl. Therm. Eng.* **2007**, *27*, 1457–1466. [CrossRef]

42. Guezennec, Y.G.; Hamama, W. *Two-Zone Heat Release Analysis of Combustion Data and Calibration of Heat Transfer Correlation in an I. C. Engine*; SAE International: Pittsburgh, PA, USA, 1999. [CrossRef]
43. Ghiji, M.; Edmonds, S.; Moinuddin, K. A Review of Experimental and Numerical Studies of Lithium Ion Battery Fires. *Appl. Sci.* **2021**, *11*, 1247. [CrossRef]
44. Catapano, F.; Perozziello, C.; Vaglieco, B.M. Heat transfer of a Stirling engine for waste heat recovery application from internal combustion engines. *Appl. Therm. Eng.* **2021**, *198*, 117492. [CrossRef]
45. Margot, X.; Quintero, P.; Gomez-Soriano, J.; Escalona, J. Implementation of 1D–3D integrated model for thermal prediction in internal combustion engines. *Appl. Therm. Eng.* **2021**, *194*, 117034. [CrossRef]
46. Yan, Z.; Gainey, B.; Lawler, B. A parametric modeling study of thermal barrier coatings in low-temperature combustion engines. *Appl. Therm. Eng.* **2021**, *200*, 117687. [CrossRef]
47. Galindo, J.; Serrano, J.R.; Arnau, F.J.; Piqueras, P. Description of a Semi-Independent Time Discretization Methodology for a One-Dimensional Gas Dynamics Model. *J. Eng. Gas Turbines Power* **2009**, *131*, 034504. [CrossRef]
48. Martin, J.; Arnau, F.; Piqueras, P.; Auñon, A. *Development of an Integrated Virtual Engine Model to Simulate New Standard Testing Cycles*; SAE International: Pittsburgh, PA, USA, 2018. [CrossRef]
49. Richards, K.J.; Senecal, P.K.; Pomraning, E. *CONVERGE 2.4*; Convergent Science: Madison, WI, USA, 2023.
50. Broatch, A.; Novella, R.; García-Tíscar, J.; Gomez-Soriano, J. Potential of dual spray injectors for optimising the noise emission of gasoline partially premixed combustion in a 2-stroke HSDI CI engine. *Appl. Therm. Eng.* **2018**, *134*, 369–378. [CrossRef]
51. Broatch, A.; Novella, R.; García-Tíscar, J.; Gomez-Soriano, J.; Pal, P. Analysis of combustion acoustic phenomena in compression–ignition engines using large eddy simulation. *Phys. Fluids* **2020**, *32*, 085101. [CrossRef]
52. Issa, R. Solution of the implicitly discretised fluid flow equations by operator-splitting. *J. Comput. Phys.* **1986**, *62*, 40–65. [CrossRef]
53. Yakhot, V.; Orszag, S.A. Renormalization group analysis of turbulence. I. Basic theory. *J. Sci. Comput.* **1986**, *1*, 3–51. [CrossRef]
54. Amsden, A.A.; Findley, M. *KIVA-3V: A Block-Structured KIVA Program for Engines with Vertical or Canted Valves*; Los Alamos National Laboratory: Los Alamos, NM, USA, 1997. [CrossRef]
55. Torregrosa, A.J.; Olmeda, P.; Degraeuwe, B.; Reyes, M. A concise wall temperature model for DI Diesel engines. *Appl. Therm. Eng.* **2006**, *26*, 1320–1327. [CrossRef]
56. Woschni, G. *A Universally Applicable Equation for the Instantaneous Heat Transfer Coefficient in the Internal Combustion Engine*; SAE Technical Paper; SAE International: Warrendale, PA, USA, 1967. [CrossRef]
57. Hohenberg, G.F. *Advanced Approaches for Heat Transfer Calculations*; SAE International: Warrendale, PA, USA, 1979; Available online: http://www.jstor.org/stable/44699090 (accessed on 12 November 2022).
58. Annand, W.J.D.; Thermodynamics and Fluid Mechanics Group. Heat Transfer in the Cylinders of Reciprocating Internal Combustion Engines. *Proc. Inst. Mech. Eng.* **1963**, *177*, 973–996. [CrossRef]
59. Blair, G.P. *Design and Simulation of Four-Stroke Engines*; SAE International: Warrendale, PA, USA, 1999.